Published in final edited form as:
J Nanopart Res. 2014 October ; 16(10): 2625–. doi:10.1007/s11051-014-2625-6.

Measuring the Soret coefficient of nanoparticles in a dilute suspension

Chao Zhao[a], **Jinxin Fu**[b], **Alparslan Oztekin**[c], and **Xuanhong Cheng**[a,*]

[a]Department of Materials Science and Engineering and Bioengineering Program, Lehigh University, Bethlehem, PA

[b]Department of Physics, Lehigh University, Bethlehem, PA

[c]Department of Mechanical Engineering and Mechanics, Lehigh University, Bethlehem, PA

Abstract

Thermophoresis is an efficient process for the manipulation of molecules and nanoparticles due to the strong force it generates on the nanoscale. Thermophoresis is characterized by the Soret coefficient. Conventionally, the Soret coefficient of nanosized species is obtained by fitting the concentration profile under a temperature gradient at the steady state to a continuous phase model. However, when the number density of the target is ultralow and the dispersed species cannot be treated as a continuous phase, the bulk concentration fluctuates spatially, preventing extraction of temperature-gradient induced concentration profile. The present work demonstrates a strategy to tackle this problem by superimposing snapshots of nanoparticle distribution. The resulting image is suitable for the extraction of the Soret coefficient through the conventional data fitting method. The strategy is first tested through a discrete phase model that illustrates the spatial fluctuation of the nanoparticle concentration in a dilute suspension in response to the temperature gradient. By superimposing snapshots of the stochastic distribution, a thermophoretic depletion profile with low standard error is constructed, indicative of the Soret coefficient. Next, confocal analysis of nanoparticle distribution in response to a temperature gradient is performed using polystyrene nanobeads down to 1e-5% (*v/v*). The experimental results also reveal that superimposing enhances the accuracy of extracted Soret coefficient. The critical particle number density in the superimposed image for predicting the Soret coefficient is hypothesized to depend on the spatial resolution of the image. This study also demonstrates that the discrete phase model is an effective tool to study particle migration under thermophoresis in the liquid phase.

Keywords

discrete phase model; nanoparticles; thermophoresis; Soret coefficient

Introduction

Thermophoresis refers to the migration of molecules and particles in response to a temperature gradient. It has found applications in various fields such as isotope

*Author to whom correspondence should be addressed: xuc207@lehigh.edu.

concentration and gas phase separation (Debye 1939; Furry et al. 1939), and has attracted a lot of research interest for the understanding of origin of life (Baaske et al. 2007; Budin et al. 2009; Mast et al. 2013), protein interactions (Wienken et al. 2010) and colloid interfacial energies (Duhr and Braun 2006b). Two parameters are commonly used to characterize thermophoresis: the thermal diffusion coefficient, D_T, which is the ratio of the thermophoretic velocity to the temperature gradient and the Soret coefficient, S_T, which is the ratio of the thermal diffusion coefficient to the normal diffusion coefficient.

There have been several proposed theories to predict the Soret coefficient (Gaeta 1969; Ruckenstein 1981; Andreev 1988; Anderson 1989; Morozov 1999; Bringuier and Bourdon 2003; Semenov and Schimpf 2004; Duhr and Braun 2006a). Because these theories are based on thermodynamic analysis of ion distribution and hydration layer structure in a temperature gradient, it is still difficult to derive the theoretical S_T due to the lack of thermodynamic parameters. Instead, S_T is mostly obtained experimentally. When the motion of the target species can be directly tracked by an optical microscope, the thermophoretic velocity and S_T is usually measured from the particle velocity. On the other hand, the measurement of S_T relies on the concentration profile. At the steady state, a balance between thermodiffusion and ordinary diffusion leads to a predictable concentration gradient in response to a temperature gradient. Assuming the diffusion and thermodiffusion coefficients are both constants and the temperature gradient is linear, the steady state concentration for two dimensional thermophoresis can be approximated by the exponential depletion law:

$$\frac{c}{c_0}=\exp[-S_T(T-T_0)] \quad (1)$$

where the normalized concentration c/c_0 depends on the temperature difference $T - T_0$. Here c_0 is the bulk concentration of the reservoir and T_0 is the ambient temperature. To extract S_T from a three dimensional concentration profile or from solute distribution in the transient state, a continuous phase model has been constructed that couples flux from convection, diffusion and thermodiffusion (Debye 1939; Furry et al. 1939; Duhr and Braun 2006a). These data-fitting methods require the target species to be in a continuum phase to measure the concentration distribution. However, when the concentration of the dispersed phase is low, the spatial distribution appears discrete and it is difficult to directly apply the depletion law or continuous phase model to obtain S_T.

To overcome this challenge, we demonstrate here that by superimposing snapshots of the nanoparticle distributions, a thermophoretic depletion profile with low standard error can be obtained for the extraction of S_T. A discrete phase model is constructed first to illustrate the stochastic nature of nanoparticle distribution in a dilute suspension and the power of overlapping to significantly reduce the spatial fluctuation of concentration. The modeling results are confirmed using polystyrene nanoparticle suspensions at a concentration down to 1e-5% (*v/v*), i.e. on the order of 32 pM. Through the combined experimental and computational analysis, we also discuss the critical particle number density to obtain accurately.

Materials

BCECF acid (2′, 7′-Bis-(2-Carboxyethyl)-5-(and-6)-Carboxyfluorescein), glass coverslips, spherical shaped polystyrene nanoparticles and mineral oil were purchased from Fisher Scientific (Fair Lawn, NJ). The nanoparticles are 100 nm in diameter and internally dyed with Firefli™ Fluorescent Red (Ex 542/Em 612 nm). The nanoparticles have a narrow size distribution and are well dispersed in the suspension. Chromium 100 nm in thickness is deposited on glass coverslips by e-beam evaporation.

Experimental Procedure

The optical set up used in this work was modified based on the literature (Jiang et al. 2009). Briefly, polystyrene nanoparticles were diluted in DI water and 3 μL of the nanoparticle suspension was pipetted on a glass slide. A chromium coated coverslip was placed on the suspension to form a 6 μm thick thin film. The edge of the coverslip was sealed by mineral oil to prevent evaporation (Duhr et al. 2004). To create a temperature gradient, an infrared laser (1 mW) was focused on the chromium layer (Fig. 1). The IR laser was a Gaussian beam with a radius around 1 μm. The temperature gradient in the liquid was calibrated independently using a temperature sensitive dye BCECF at a concentration of 1 mM (Maeda et al. 2012). The fluorescence intensity of BCECF decreases linearly with temperature (Fig. S1). The particle distribution was imaged using confocal microscopy on the center plane between the two solid substrates.

Mathematical Model and Numerical Method

Numerical analysis was performed by both continuous and discrete phase models. In both models, the power density of the IR laser was modeled as a three dimensional Gaussian distribution and the laser was considered as an energy source:

$$Q=Q_0(1-R_c)A_c\left(\frac{1}{\pi r_x r_y}\right)\exp\left(-\frac{(x-x_0)^2}{2r_x^2}-\frac{(y-y_0)^2}{2r_y^2}\right)\exp(A_c abs(z)) \quad (2)$$

where Q is the power density in the fluid, Q_0 is the total laser power, A_c is absorption coefficient, R_c is reflection coefficient, r_x and r_y are the beam waist of laser pulse in the x and the y directions, respectively. x_0 and y_0 are the center coordinates of the laser beam, and x, y, and z are the spatial coordinates. $abs(z)$ is the absolute value of z. Since the liquid film is thin, the laser heating established a two dimensional temperature gradient in the liquid between the focal point and the ambient (Fig. S2).

For the continuous phase model, the governing equations to describe natural convection are the Navier-Stokes equation with Boussinesq approximation and the mass conservation equation:

$$\frac{\partial \boldsymbol{u}}{\partial t}+\boldsymbol{u}\cdot\nabla\boldsymbol{u}=-\frac{1}{\rho}\nabla p+\gamma\nabla^2\boldsymbol{u}+\alpha\boldsymbol{g}(T-T_0) \quad (3)$$

$$\nabla \cdot (\rho \boldsymbol{u}) = 0 \quad (4)$$

where ρ is the fluid density, γ is the kinematic viscosity, t is the time, $\boldsymbol{u}$ is the fluid velocity, p is the pressure, α is the thermal expansion coefficient of the fluid, $\boldsymbol{g}$ is the gravitational acceleration, and T is the temperature.

The conservation of energy is in the form:

$$\rho C_p \frac{\partial T}{\partial t} + \rho C_p \boldsymbol{u} \cdot \nabla T = \nabla \cdot (k \nabla T) \quad (5)$$

where C_p is the heat capacity of the fluid, and k is the thermal conductivity of the fluid.

The mass transport equation includes the mass diffusion, advection and the effect of the thermophoresis:

$$\frac{\partial c}{\partial t} = \nabla \cdot (D_T c \nabla T + D \nabla c) - \nabla \cdot (\boldsymbol{u} c) \quad (6)$$

where c is the concentration of the species.

The discrete phase model employed the particle tracking theory with Eulerian-Lagrangian approach. The solvent (continuous phase) was treated using Eulerian description and the dispersed particles (discrete phase) were tracked using the Lagrangian description. Two-way coupling was employed in our modeling, where the continuous phase could affect the behavior of discrete phase, and vice versa. Hence, in this process a proper designed solver calculated the continuous and discrete phase equations in an alternate manner until a converged coupled solution was achieved. Particles were treated as volumeless points, but the size effect was incorporated in the Brownian, the drag, the lift and the buoyancy forces exerted on the particles. Given the low particle concentration and much larger detection volume compared to the particle size, particle-particle and particle-wall interactions are negligible. Thus, it is reasonable to ignore the particle volume for particle tracking.

By employing Eulerian approach, the steady creeping fluid flow was modeled by Navier-Stokes equation including the source term. The equations governing the conservation of mass and momentum of the liquid phase are (Drew 1983; Zhang and Prosperetti 1997)

$$\nabla \cdot (\rho \boldsymbol{u}) = 0 \quad (7)$$

$$\nabla \cdot (\rho \boldsymbol{u}\boldsymbol{u}) = -\nabla p + \nabla \cdot (\bar{\bar{\tau}}) + \rho \boldsymbol{g} + \frac{1}{V_{ijk}} \sum_p \left(F_D (\boldsymbol{u_p} - \boldsymbol{u}) \right) \dot{m}_p \Delta t \quad (8)$$

$$\mathrm{Re}_r=\frac{\rho d_p|\boldsymbol{u_p}-\boldsymbol{u}|}{\mu}\ and\quad F_D=\frac{18\mu}{\rho_P d_p^2}\frac{C_D\mathrm{Re}_r}{24} \quad (9)$$

where ρ is the fluid density, μ is the viscosity of the fluid, $\boldsymbol{u}$ is the fluid phase velocity, p is the static pressure, $\bar{\bar{\tau}}$ is the stress tensor, $\rho\boldsymbol{g}$ is the gravitational body force, $\boldsymbol{u_p}$ is the particle velocity, ρ_P is the density of the particle, d_p is the particle diameter, C_D is the drag coefficient, $\dot{m}_p$ is the mass flow rate of the particles, Δt is the time step, $F_D(\boldsymbol{u_p}-\boldsymbol{u})$ is the drag force per unit particle mass and Re_r is the relative Reynolds number. The last term in the Eq. 8 is the momentum source term that represents the influence of the particles on the flow field of fluids. It is calculated by averaging momentum of all the particles in the volume of fluid element (V_{ijk}).

Lagrangian approach was employed for the discrete phase model to track the movement of particles (Anderson 1989; Li and James 1995; Bielenberg and Brenner 2005; Guha 2008):

$$\frac{d\boldsymbol{u_p}}{dt}=F_D(\boldsymbol{u}-\boldsymbol{u_p})+\frac{\boldsymbol{g}(\rho_p-\rho)}{\rho_p}+\boldsymbol{F_b}+\boldsymbol{F_l}+\boldsymbol{F_{tp}} \quad (10)$$

$$\boldsymbol{F_b}=\boldsymbol{\zeta}\sqrt{\frac{\pi S_0}{\Delta t}}\ and\ S_0=\frac{216\mu k_B T}{\pi^2\rho^2 d_p^5\left(\frac{\rho_p}{\rho}\right)^2 C_c} \quad (11)$$

$$\boldsymbol{F_l}=\frac{2K(\mu/\rho)^{1/2}\rho\bar{\bar{d}}}{\rho_p d_p(\bar{\bar{d}}:\bar{\bar{d}})^{1/4}}\cdot(\boldsymbol{u}-\boldsymbol{u_p}) \quad (12)$$

$$\boldsymbol{F_{tp}}=6\pi\mu d_p\boldsymbol{u}=-6\pi\mu d_p D_T\nabla T \quad (13)$$

where $\boldsymbol{F_b}$ is the Brownian force per unit particle mass (Li and Ahmadi 1992), $\boldsymbol{F_l}$ is the Saffman's lift force per unit particle mass due to shear (Saffman 1965), the thermophoretic force per unit particle mass in liquid $\boldsymbol{F_{tp}}$ is modeled using the empirical Stokes law (Bielenberg and Brenner 2005), K=2.594, $\boldsymbol{\zeta}$ are zero-mean, unit-variance-independent Gaussian random number composed vector, T is the absolute temperature of the fluid, k_B is the Boltzmann constant, C_c is the Stokes-Cunningham slip correction, and $\bar{\bar{d}}$ is the deformation rate tensor. Temperature distribution in the fluid is determined by solving the energy equation displayed in equation 5. Iterative calculations to solve Navier-Stokes equations were carried out by the SIMPLE scheme for pressure-velocity coupling.

The continuous phase model was implemented using COMSOL (Burlington, MA). The transport of species model was modified to include the thermophoretic flux term $D_T c\nabla T$ (Duhr and Braun 2006a) and solved together with laminar flow and heat transfer models. For discrete phase model, ANSYS Fluent (Canonsburg, PA) was employed to simulate heat transfer, laminar flow, and particle tracking in 3D (Zhao et al. 2013). Nanoparticles with a diameter of 100 nm were randomly injected in the 3D microfluidic chamber. For both cases,

the proper mesh size was confirmed to attain a spatial convergence. All data were acquired at the quasi-steady state. All the parameters in the simulation is listed in Table 1.

Results and Discussions

In response to a temperature gradient, thermophobic species move away from the high temperature region. The continuous phase model predicts that the steady-state concentration follows an exponential depletion law (Eq. 1) controlled by S_T. The image in Fig. 2(a) shows a simulated concentration contour at the steady state by the continuous phase model. The simulated volume is 360 μm × 360 μm × 6 μm and the center plane (z = 3 μm) with an area of 120 μm × 120 μm is analyzed here to avoid boundary artifacts. Since the height is only 6 μm, natural convection in the z-direction is negligible (Duhr et al. 2004), so a 2D distribution profile in the x-y plane is expected. S_T of 0.18 1/K is used in the simulation, which was previously reported for 100 nm polystyrene particles in water (Duhr and Braun 2006a). The radially averaged concentration profile (Fig. 2a, bottom) is smooth, corresponding to a continuous phase distribution. Fitting the non-zero region of the distribution to the exponential depletion law (Eq. 1), a Soret coefficient of 0.18 ± 0.002 1/K is obtained, matching the set value for the simulation.

When the target is considered as a discrete species, its concentration is expected to fluctuate in space. To demonstrate this effect, a discrete phase model was set up using parameters relevant to 100 nm polystyrene particles. This model was firstly used to validate against the continuous phase model using a high particle concentration of 1% (*v/v*) (Fig. 2b), which yields ∼1 million particles in the region of interest (ROI). The concentration fluctuation in the bulk is much smaller than the difference generated by the temperature gradient, thus the radially averaged concentration profile is smooth and the extracted Soret coefficient matches the set value.

When the particle concentration is reduced to 1e-4% (*v/v*) in the discrete phase model, the concentration fluctuation in the bulk is at a comparable level to the difference generated by the temperature gradient (Fig. 2c). Here, ∼180 particles are present in the ROI, which is much less than the mesh number of ∼15,000. The instantaneous concentration contour shows the location of individual particles, while a large volume in the bulk has no particle. Thus, the thermophoretic depletion in the center is much less obvious. Even after radial averaging, the bulk distribution is not smooth. Fitting the averaged concentration to Eq. 1 results in a Soret coefficient of 0.21 ± 0.03 1/K, which is 16% higher than expected.

To increase the number density of targets in the ROI for a low concentration sample, snapshots of concentration contours from the discrete phase model were superimposed. The number density is the summation of particle number over several snapshots divided by the surface area. Mathematically, the number density is the multiplication of particle number density on a plane and the number of snapshots. Images were acquired in the x-y plane at z = 3 μm with a time interval of 1 second after the particle distribution in the discrete phase model reached a quasi-steady state. Similar to the Kalman filter, the signal to noise ratio, which is the ratio between coefficient estimate and respective standard error, is expected to improve with this practice. The depletion in the center is much more obvious for 250

overlays compared to a single snapshot (Fig. 3a, b). Fig. 3c-f shows the radially averaged concentration profile for different numbers of overlays of 10, 50 and 250. The concentration profiles become smoother and the depletion center is more pronounced with the numbers of overlays. For the overlays of 250 images, the derived S_T is 0.18 ± 0.003 1/K, matching the set value of 0.18 1/K for the simulation.

Since the discrete phase model supports construction of a low standard error depletion profile by superimposing, experiments were carried out to validate the procedure. Polystyrene beads at a concentration of 1e-4% (*v/v*), i.e. 320 pM were used first, comparable to that in the simulation. A liquid film 6 μm thick was constrained between a chromium coated coverslip and a glass slide. Images were taken 3 μm above the bottom glass slide. Similar to the simulation, fluorescence images were acquired every second after the system reached quasi-steady state. Similar to Fig. 3a and 3b, Fig. 4a and 4b show the confocal fluorescence images for one snapshot versus 250 overlays. In the single snapshot, the particle distribution is stochastic and the depletion center is hard to visualize. After 250 overlays, the depletion in the center is pronounced. Fig. 4c-f shows the radially averaged concentration profiles for different numbers of overlays in the experiments. For single snapshot, the extracted S_T is 0.16 ± 0.03 1/K. The S_T becomes 0.18 ± 0.006 1/K with 250 overlays, which matches the previous reported value (Duhr and Braun 2006a). When a coefficient estimate is defined as the extracted S_T and standard error is from the smooth fitting, the signal to noise ratio is about 5 for the single snapshot and 30 for 250 overlays.

When the particle concentration is further decreased to 1e-5% (*v/v*), i.e. 32 pM, more numbers of overlays are needed to accurately determine the Soret coefficient (Fig. 5). For a single snapshot, no thermophoretic depletion is observable even in the radially averaged concentration profile (Fig. 5a). When 10 images are stacked (Fig. 5b), the depletion is barely observable, and the extracted S_T is 0.23 ± 0.06 1/K. This number deviates from the known value of 0.18 1/K, and the high standard error roots from a sparse particle distribution. When 100 and 1000 images are overlaid (Fig. 5c, d), extracted S_T is 0.21 ± 0.04 1/K and 0.18 ± 0.01 1/K, respectively. The signal to noise ratio reaches ∼20 with 1000 overlays. Compared to the results from the suspension at 1e-4% (*v/v*), the suspension at 1e-5% (*v/v*) requires more overlays to yield a comparable signal to noise ratio.

To compare all the data described above, we calculated particle number density in the ROI. Fig. 6 shows the extracted Soret coefficients as a function of the particle number density from all the simulation and experimental data above. The dash line represents the expected value. The experimental result from a single snapshot at a concentration of 1e-5% is not included as the signal to noise ratio is 5e-6. For all other cases, the signal to noise ratio is greater than 3.

When the particle number density is equal to or less than 0.06 μm^{-2}, the Soret coefficient extracted from the radial concentration profile deviates from the expected value by more than 20%. The large error bar indicates great fluctuation of the spatial concentration in these measurements. When the particle number density is 0.06 μm^{-2}, whether it is by increasing the suspension concentration (data not shown) or by image superimposing, the Soret coefficient converges to within 99% of the expected value with a standard error of ∼0.002

1/K. More overlays generally reduce the standard error even more, since the scattered behavior is averaged and the standard deviation is inversely proportional to square root of sample number.

One possible explanation to the threshold of the particle number density to accurately predict S_T arises from the microscope resolution. When the particle number density is greater than 0.06 μm^{-2}, the average particle-particle distance is < 4 μm. This is on the same order as the spatial resolution of the microscope and nanoparticle size used in our work, thus the particle can be approximated as a continuous phase to apply the exponential depletion law. Long exposure of the sample may also result in the averaging effect, but continuous exposure may lead to sample bleaching and undesirable heating by the imaging light source.

To our knowledge, this work is the first that applies the discrete phase model to study nanoparticle thermophoresis in a liquid suspension. Discrete phase models have long been developed to understand contamination in the cleanroom and soot entrainment in the gas phase (Longest and Xi 2007; Woo et al. 2012; Majlesara et al. 2013; Tan et al. 2013; Lee and Yook 2014). The thermophoretic force on aerosol particles in the gas phase is modeled using the equation proposed by L. Talbot *et al.* (Talbot et al. 1980), which is directly proportional to the particle diameter, gas kinematic viscosity and inversely proportional to the particle mass. However, the relationship is not valid in the liquid phase and theoretical prediction of S_T in the liquid phase is not yet available. Instead, thermophoretic force is implemented by the empirical Stokes law here. When coupled with the hydrodynamic and Brownian forces, the resulting discrete phase model provides an effective tool to study the distribution of nanoparticles at ultralow concentrations. As other non-conservative force fields and particle-particle interactions can be included, this discrete phase model is expected to find broad utility to study complex nanoparticle migration under thermophoresis in a liquid suspension.

Conclusions

We present an approach here to measure the Soret coefficient of a highly diluted species in a liquid suspension. By superimposing distribution images of the dispersed species, a smooth concentration profile matching the depletion law is constructed and the Soret coefficient is extracted accurately. This approach is validated using both discrete phase models and experimental measurements. The particle number density in the superimposed image needs to be comparable to the spatial resolution of the image. The discrete phase model developed here is shown to be useful for the study of nanoparticle migration and distribution in liquids in response to a temperature gradient.

Supplementary Material

Refer to Web version on PubMed Central for supplementary material.

Acknowledgments

We are grateful for the helpful discussions about confocal microscopy with Prof. H. Daniel Ou-Yang and Ming-Tzo Wei. Funding for the research is provided by National Institute of Health under Grant No NIAID-1R21AI081638 and Pennsylvania Department of Health CURE Formula Funds.

References

Anderson JL. Colloid transport by interfacial forces. Annu Rev Fluid Mech. 1989; 21:61–99.10.1146/annurev.fluid.21.1.61

Andreev AF. Thermophoresis in liquids. Zhurnal Eksp I Teor Fiz. 1988; 94:210–216.

Baaske P, Weinert FM, Duhr S, Lemke KH, Russell MJ, Braun D. Extreme accumulation of nucleotides in simulated hydrothermal pore systems. Proc Natl Acad Sci U S A. 2007; 104:9346–9351.10.1073/pnas.0609592104 [PubMed: 17494767]

Bielenberg JR, Brenner H. A hydrodynamic/brownian motion model of thermal diffusion in liquids. Phys A Stat Mech its Appl. 2005; 356:279–293.10.1016/j.physa.2005.03.033

Bringuier E, Bourdon A. Colloid transport in nonuniform temperature. Phys Rev E. 200310.1103/PhysRevE.67.011404

Budin I, Bruckner RJ, Szostak JW. Formation of protocell-like vesicles in a thermal diffusion column. J Am Chem Soc. 2009; 131:9628–9629.10.1021/ja9029818 [PubMed: 19601679]

Debye P. Zur theorie des clusiusschen trennungsverfahrens. Ann Phys. 193910.1002/andp.19394280310

Drew DA. Mathematical-modeling of 2-phase flow. Annu Rev Fluid Mech. 1983; 15:261–291.10.1146/annurev.fl.15.010183.001401

Duhr S, Arduini S, Braun D. Thermophoresis of dna determined by microfluidic fluorescence. Eur Phys J E Soft Matter. 2004; 15:277–286.10.1140/epje/i2004-10073-5 [PubMed: 15592768]

Duhr S, Braun D. Why molecules move along a temperature gradient. Proc Natl Acad Sci U S A. 2006a; 103:19678–19682.10.1073/pnas.0603873103 [PubMed: 17164337]

Duhr S, Braun D. Optothermal molecule trapping by opposing fluid flow with thermophoretic drift. Phys Rev Lett. 2006b10.1103/PhysRevLett.97.038103

Furry W, Jones R, Onsager L. On the theory of isotope separation by thermal diffusion. Phys Rev. 1939; 55:1083–1095.10.1103/PhysRev.55.1083

Gaeta FS. Radiation pressure theory of thermal diffusion in liquids. Phys Rev. 1969; 182:289.10.1103/PhysRev.182.289

Guha A. Transport and deposition of particles in turbulent and laminar flow. Annu Rev Fluid Mech. 2008; 40:311–341.10.1146/annurev.fluid.40.111406.102220

Jiang HR, Wada H, Yoshinaga N, Sano M. Manipulation of colloids by a nonequilibrium depletion force in a temperature gradient. Phys Rev Lett. 200910.1103/PhysRevLett.102.208301

Lee H, Yook SJ. Deposition velocity of particles in charge equilibrium onto a flat plate in parallel airflow under the influence of simultaneous electrophoresis and thermophoresis. J Aerosol Sci. 2014; 67:166–176.10.1016/j.jaerosci.2013.10.006

Li A, Ahmadi G. Dispersion and deposition of spherical particles from point sources in a turbulent channel flow. Aerosol Sci Technol. 1992; 16:209–226.10.1080/02786829208959550

Li W, James Davis E. Measurement of the thermophoretic force by electrodynamic levitation: microspheres in air. J Aerosol Sci. 1995; 26:1063–1083.10.1016/0021-8502(95)00047-G

Longest PW, Xi J. Effectiveness of direct lagrangian tracking models for simulating nanoparticle deposition in the upper airways. Aerosol Sci Technol. 2007; 41:380–397.10.1080/02786820701203223

Maeda YT, Tlusty T, Libchaber A. Effects of long dna folding and small rna stem-loop in thermophoresis. Proc Natl Acad Sci U S A. 2012; 109:17972–17977.10.1073/pnas.1215764109 [PubMed: 23071341]

Majlesara M, Salmanzadeh M, Ahmadi G. A model for particles deposition in turbulent inclined channels. J Aerosol Sci. 2013; 64:37–47.10.1016/j.jaerosci.2013.06.001

Mast CB, Schink S, Gerland U, Braun D. Escalation of polymerization in a thermal gradient. Proc Natl Acad Sci U S A. 2013; 110:8030–8035.10.1073/pnas.1303222110 [PubMed: 23630280]

Morozov KI. Thermal diffusion in disperse systems. J Exp Theor Phys. 1999; 88:944–946.10.1134/1.558875

Ruckenstein E. Can phoretic motions be treated as interfacial-tension gradient driven phenomena. J Colloid Interface Sci. 1981; 83:77–81.10.1016/0021-9797(81)90011-4

Saffman PG. The lift on a small sphere in a slow shear flow. J Fluid Mech. 1965; 22:385.10.1017/S0022112065000824

Semenov S, Schimpf M. Thermophoresis of dissolved molecules and polymers: consideration of the temperature-induced macroscopic pressure gradient. Phys Rev E. 200410.1103/PhysRevE.69.011201

Talbot L, Cheng RK, Schefer RW, Willis DR. Thermophoresis of particles in a heated boundary-layer. J Fluid Mech. 1980; 101:737–758.10.1017/s0022112080001905

Tan SM, Ng HK, Gan S. Cfd modelling of soot entrainment via thermophoretic deposition and crevice flow in a diesel engine. J Aerosol Sci. 2013; 66:83–95.10.1016/j.jaerosci.2013.08.007

Wienken CJ, Baaske P, Rothbauer U, Braun D, Duhr S. Protein-binding assays in biological liquids using microscale thermophoresis. Nat Commun. 2010; 1:100.10.1038/ncomms1093 [PubMed: 20981028]

Woo SH, Lee SC, Yook SJ. Statistical lagrangian particle tracking approach to investigate the effect of thermophoresis on particle deposition onto a face-up flat surface in a parallel airflow. J Aerosol Sci. 2012; 44:1–10.10.1016/j.jaerosci.2011.10.003

Zhang DZ, Prosperetti A. Momentum and energy equations for disperse two-phase flows and their closure for dilute suspensions. Int J Multiph Flow. 1997; 23:425–453.10.1016/S0301-9322(96)00080-8

Zhao C, Oztekin A, Cheng X. Gravity-induced swirl of nanoparticles in microfluidics. J Nanoparticle Res. 201310.1007/s11051-013-1611-8

Nomenclature

x, y, z (μm)	Spatial coordinates
D_T (μm ^{2} s $^{-1}$ K $^{-1}$)	The thermal diffusion coefficient
S_T (K^{-1})	The Soret coefficient
D (μm^2 s^{-1})	The diffusion coefficient
c (kg m^{-3})	Concentration of the nanoparticles
T (K)	Absolute temperature of the fluid
Q (mW m^{-3})	Power density
Q_0 (mW)	The laser power
A_c (m^{-1})	Absorption coefficient
R_c	Reflection coefficient
r_x (μm)	Laser pulse x standard deviation
r_y (μm)	Laser pulse y standard deviation
ρ (kg m^{-3})	Density of the fluid phase
u (m s^{-1})	Velocity of the fluid phase
Δt (s)	Time step
μ (Pa s)	Dynamic viscosity of the fluid
γ (m^2 s^{-1})	Kinematic viscosity of the fluid
p (Pa)	Static pressure

α (K^{-1})	Thermal expansion coefficient of the fluid
g (m s^{-2})	Gravitational acceleration
C_p (J kg^{-1} K^{-1})	Heat capacity of the fluid
k (W m^{-1} K^{-1})	Thermal conductivity of the fluid
F_{tp} (m s^{-2})	Thermophoretic force per unit particle mass
ρ_p (kg m^{-3})	Density of the nanoparticles
$\dot{m}_p$ (kg s^{-1})	Mass flow rate of the particles
V_{ijk} (m^{-3})	Volume of fluid element
d_p (μm)	Diameter of the nanoparticles
u_p (m s^{-1})	Velocity of the nanoparticles
$\bar{\bar{\tau}}$ (Pa)	Stress tensor
$F_D(u - u_p)$ (m s^{-2})	Drag force per unit particle mass
Re	Reynolds number
Re_r	Relative Reynolds number
C_D	Drag coefficient
F_b (m s^{-2})	Brownian force per unit particle mass
F_l (m s^{-2})	Lift force per unit particle mass
k_B (m^2 kg s^{-2} K^{-1})	Boltzmann constant
$\bar{\bar{d}}$ (s^{-1})	Deformation rate tensor

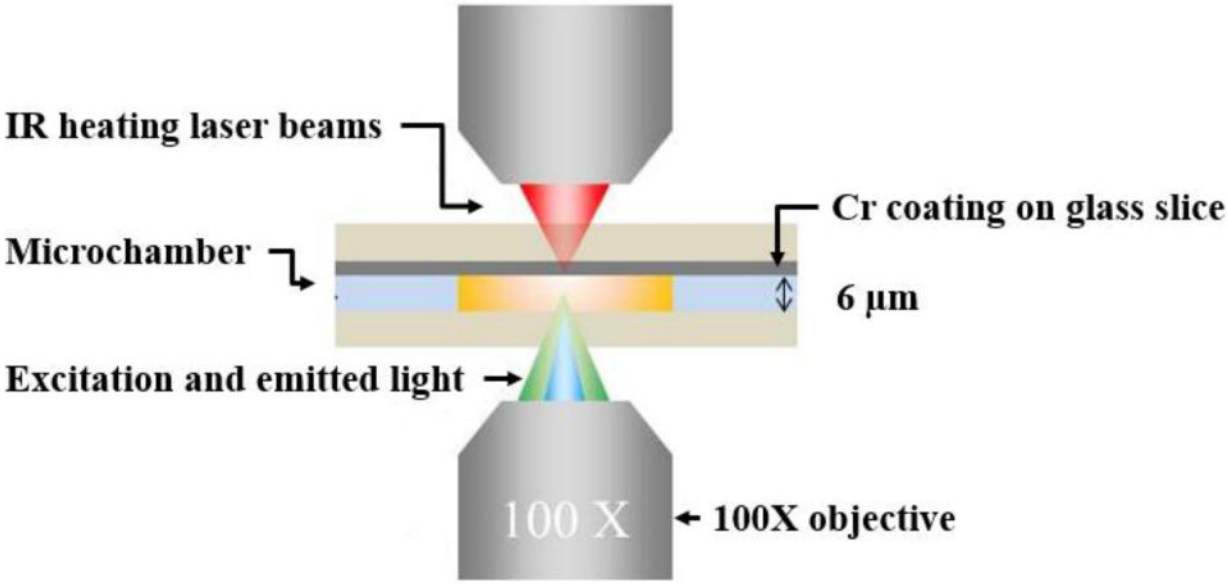

Fig. 1.

A schematic of the optical setup combined with a microfluidic chamber used in this study. The laser was focused on the ceiling with a thin chromium layer to absorb the IR energy. Distribution of 100 nm fluorescent Polystyrene beads was observed by a confocal fluorescence microscope.

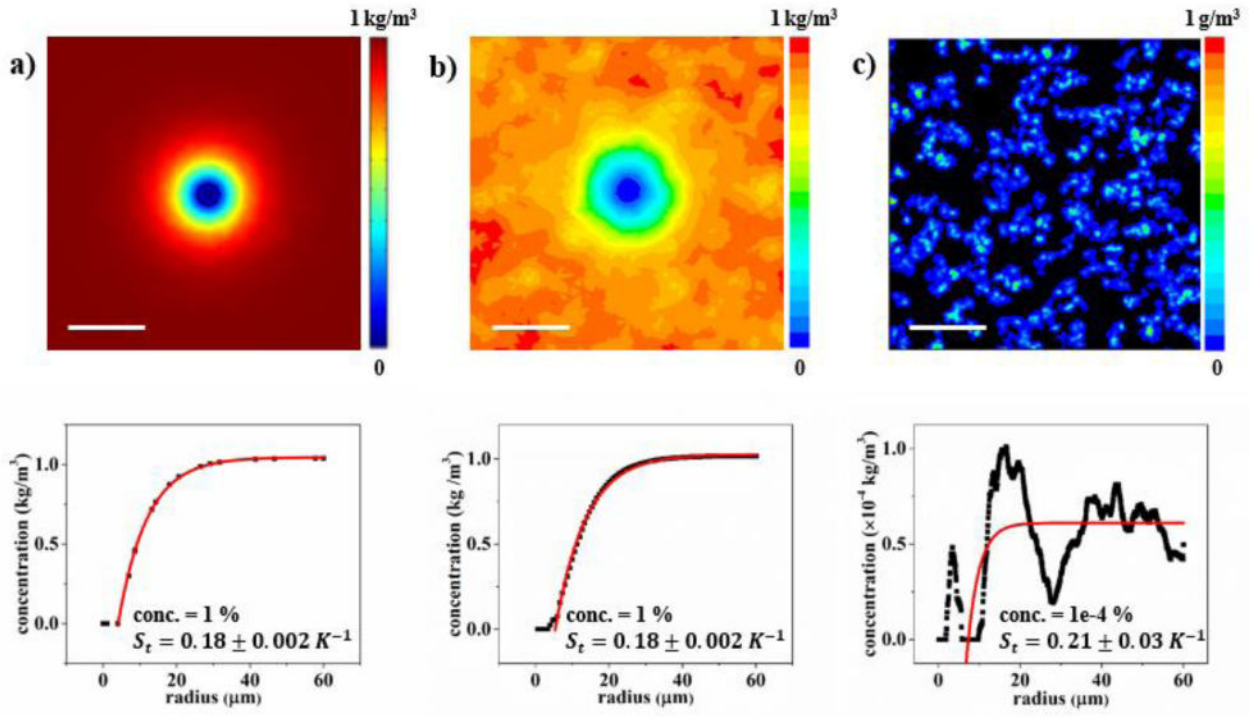

Fig. 2.

Concentration contour (top) and radially averaged concentration profile (bottom) for a) continuous phase modeling with concentration at 1% (*v/v*), b) discrete phase modeling with concentration at 1% (*v/v*), and c) discrete phase modeling with concentration at 1e-4% (*v/v*). The black dots in the bottom panel show the radially averaged concentration, and the red lines are fittings based on the depletion law in Eq. 1. Scale bars = 30 μm.

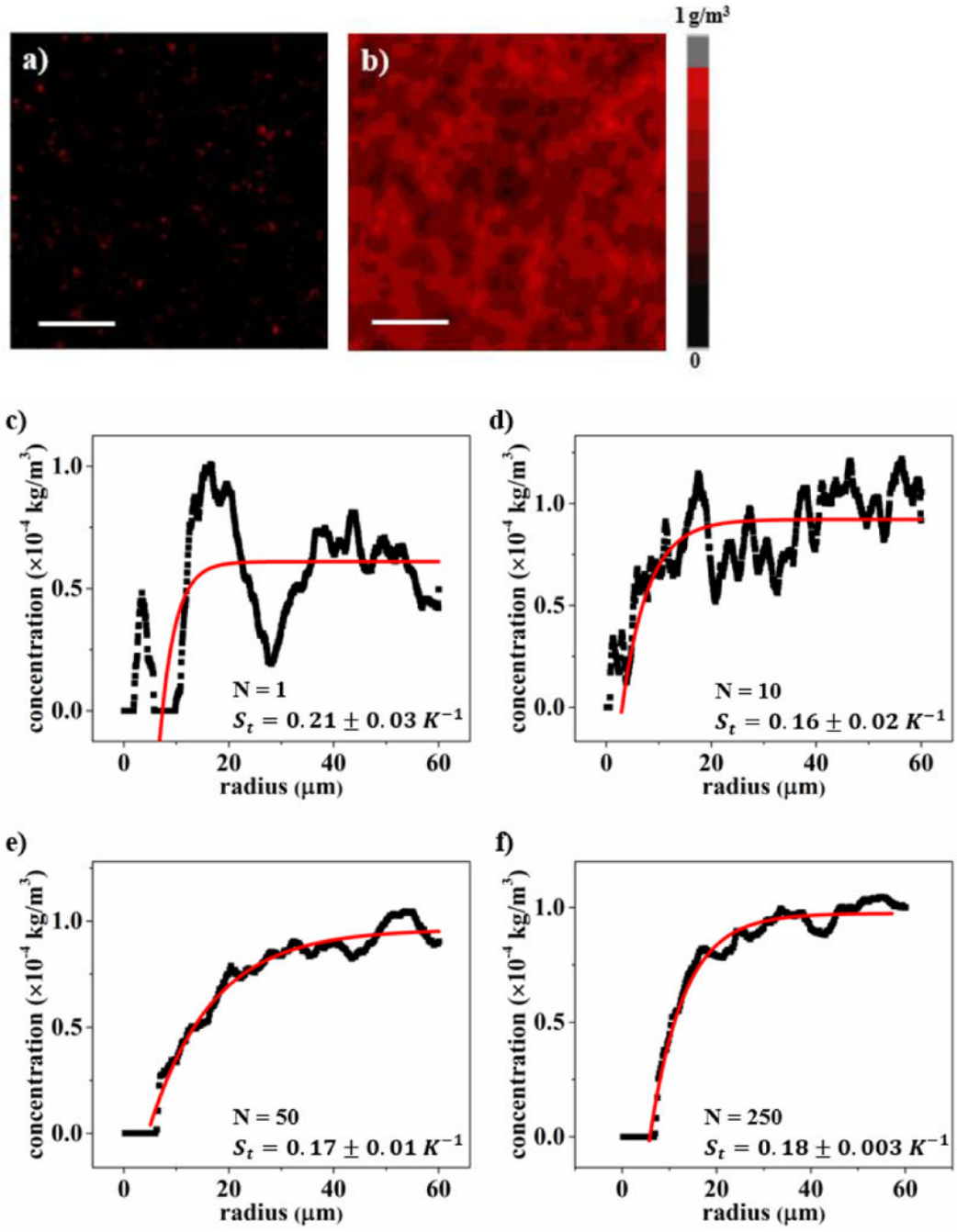

Fig. 3.

Simulated concentration contour for a) 1 snapshot and b) 250 overlays of nanoparticle distribution in response to a radially symmetric temperature gradient. Both images are 120 μm by 120 μm and the particle concentration is 1e-4% (*v/v*). Radially averaged quasi-steady concentration profiles of c) 1 snapshot, d) 10 overlays, e) 50 overlays, and f) 250 overlays from the discrete phase model. The black dots show the radially averaged concentration, and the red lines are fittings based on the depletion law in Eq. 1. Scale bars = 30 μm.

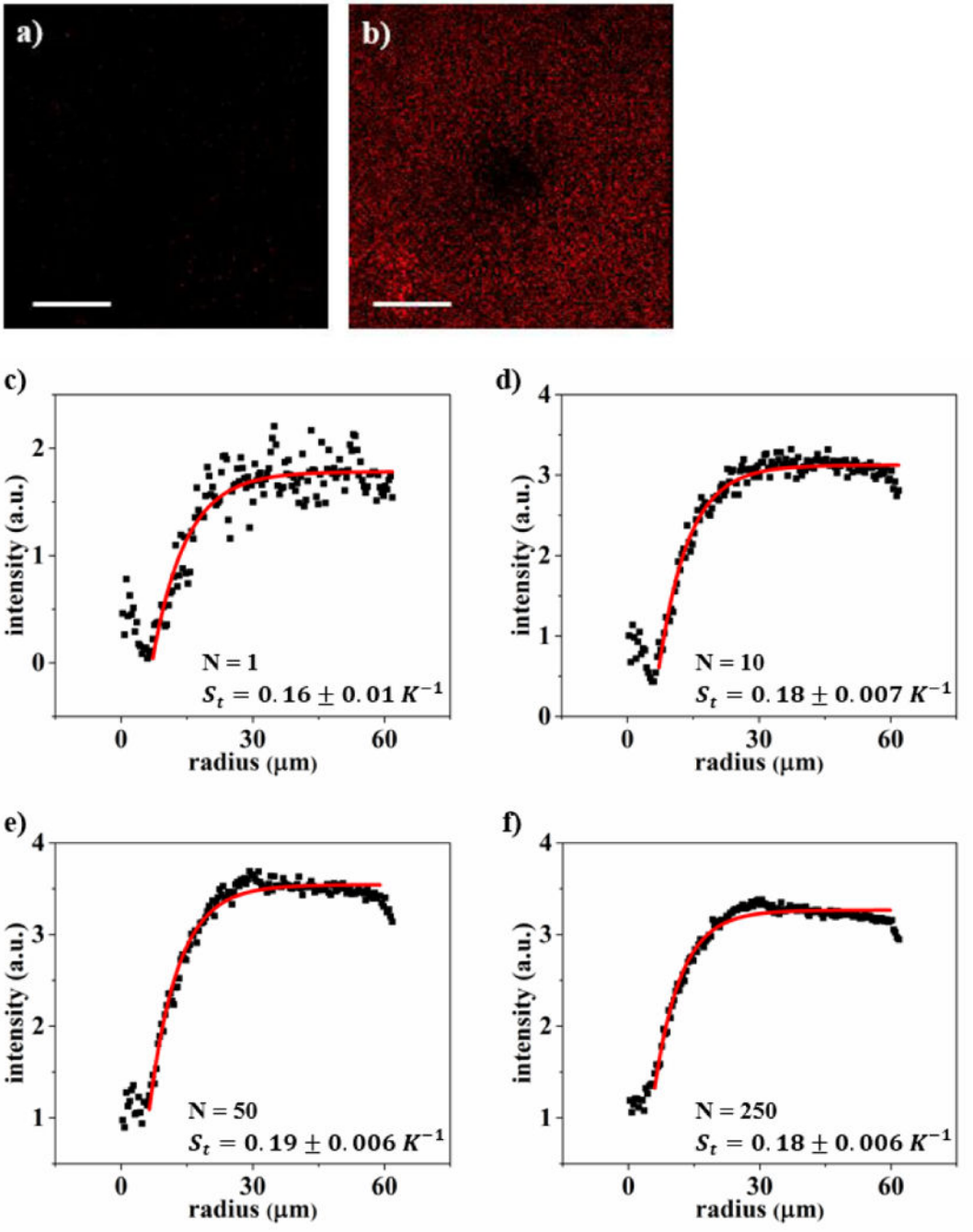

Fig. 4.

Experimentally measured distribution of 100nm polystyrene nanoparticle in response to a radially symmetric temperature gradient for a) single snapshot and b) 250 overlays. Both images are 120 μm by 120 μm. Radially averaged concentration profiles at quasi-steady state from c) single snapshot, d) 10 overlays, e) 50 overlays, and f) 250 overlays. The concentration of the polystyrene particle suspension is 1e-4% (*v/v*). The black dots show the radially averaged concentration, and the red lines are fittings based on the depletion law in Eq. 1. Scale bars = 30 μm.

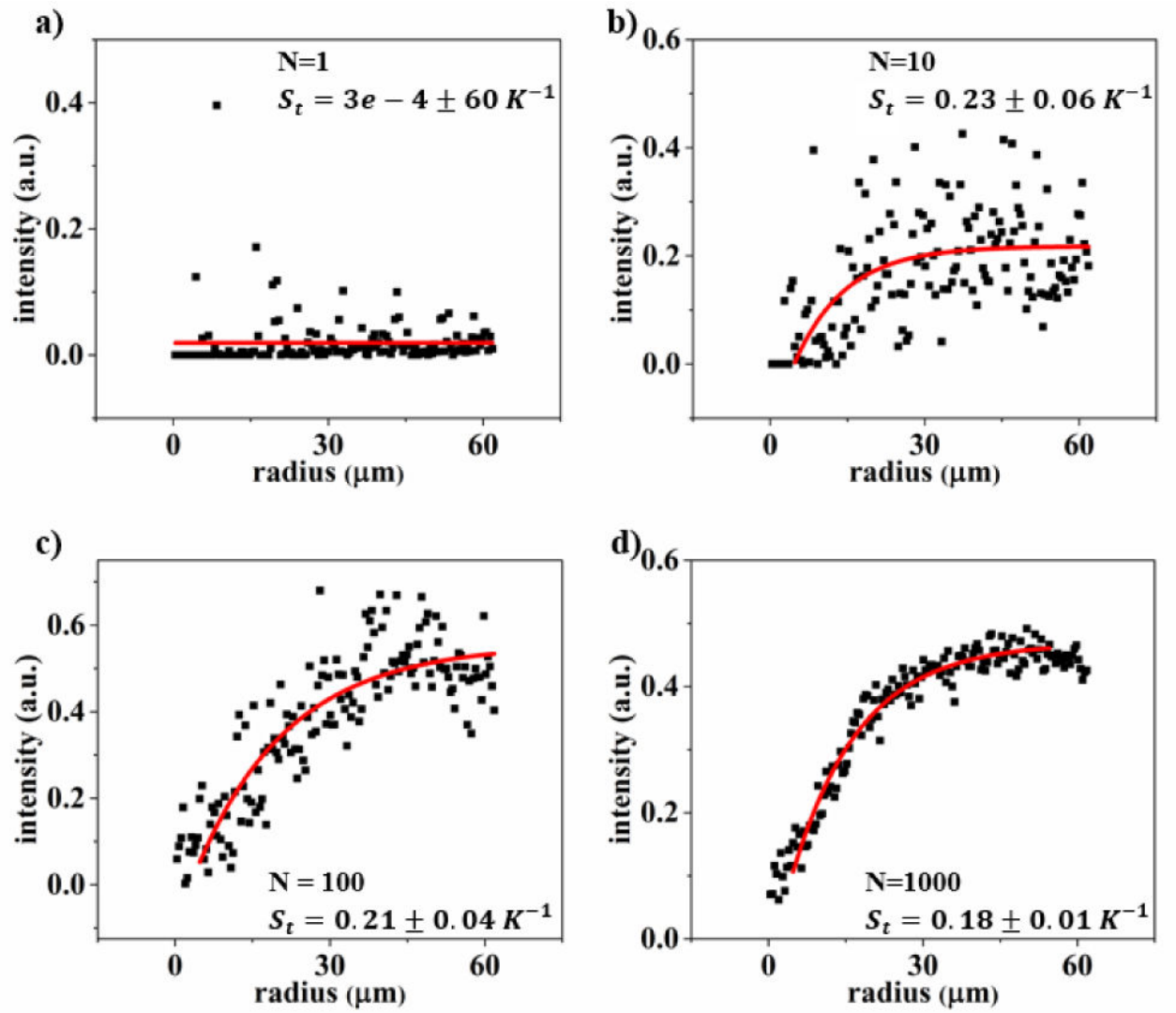

Fig. 5.

Radially averaged concentration profiles by experimental measurements at a quasi-steady state from a) single snapshot, b) 10 overlays, c) 100 overlays, and d) 1000 overlays. The concentration of the polystyrene particle suspension is 1e-5% (*v/v*). The black dots are radially averaged concentration, and the red lines are fittings based on the depletion law in Eq. 1.

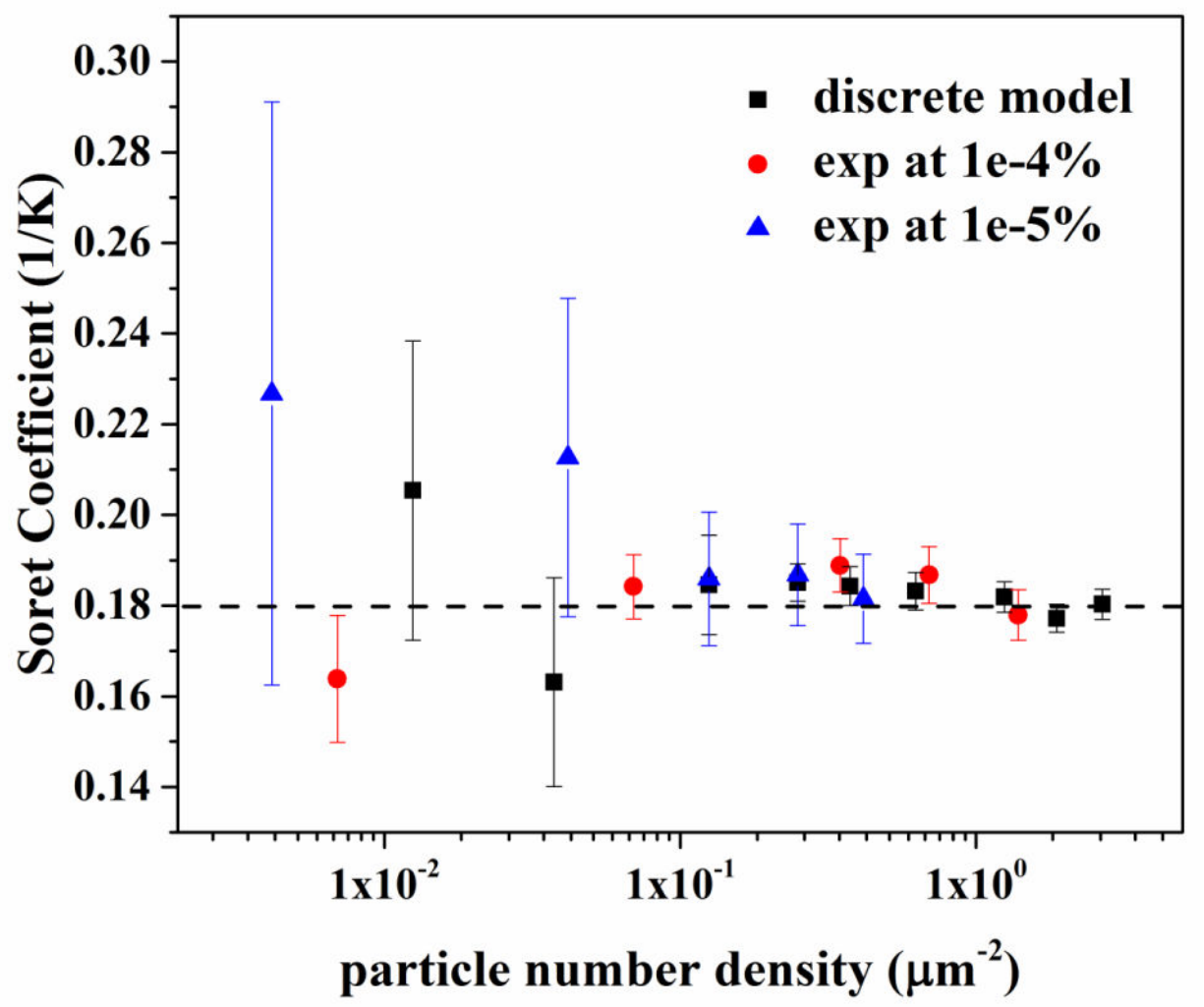

Fig. 6.

The relationship between the extracted Soret coefficients and particle number density from the discrete phase model and experiments with particle concentration of 1e-4% (*v/v*) and 1e-5% (*v/v*).

Table 1

Properties of IR laser, fluid and nanoparticles in the simulation.

Symbols	Value
Q_0	1 mW
R_c	0.56
A_c	3.67e7 m^{-1}
r_x	0.5 μm
r_y	0.5 μm
ρ	1000 kg m^{-3}
ρ_p	1050 kg m^{-3}
d_p	100 nm
μ	0.001 Pa s
γ	1e-6 m^2 s^{-1}
α	6.9e-5 K^{-1}
$\boldsymbol{g}$	9.8 m s^{-2}
C_p	4.19 J g^{-1} K^{-1}
k	0.58 W m^{-1} K^{-1}
D_T	0.792 μm^2 s^{-1} K^{-1}
S_T	0.18 K^{-1}
D	4.4 μm^2 s^{-1}